Dual-band higher-order topological states in composite square-lattice sonic crystals

Shi-Jie Cui,[1] Zhi-Guo Geng,[1,*] Zhaojiang Chen,[1] Ya-Xi Shen,[1] and Xue-Feng Zhu[2,†]

[1] *Department of Physics, Zhejiang Normal University, Jinhua, Zhejiang 321004, People's Republic of China*
[2] *School of Physics and Innovation Institute, Huazhong University of Science and Technology, Wuhan, Hubei 430074, People's Republic of China*

(Received 21 October 2024; revised 23 February 2025; accepted 5 March 2025; published 3 April 2025)

The discovery of higher-order topological insulator metamaterials has enriched fundamental schemes of classical wave manipulations. A common way of inducing higher-order topological wave phenomena is based on the original C_n-symmetric lattice characterized by a quantized Wannier center, which generally supports the higher-order topological states in a single band gap. Here, we report the acoustic realization of dual-band second-order topological insulators in C_{4v}-symmetric composite lattices, created by inserting extra sites into each inversion center of four adjacent unit cells of the original two-dimensional Su-Schrieffer-Heeger lattice. Due to the hybrid operation, we can create distinct nontrivial boundaries along the inserted sites, and multiple acoustic localized states occur in two band gaps simultaneously. Relying on two square-shaped sonic crystals with nontrivial boundaries, we experimentally verify the diverse state localizations on the corners and edges of the sonic crystals, and distinct phase profiles are observed for the boundary states in different band gaps. The topological robustness of corner and edge states under bulk disorder is experimentally demonstrated in comparison with the measured spectra of relevant boundary disorders. Our work opens an avenue to develop multifrequency acoustic devices, which may facilitate useful applications of multiband acoustic sensors and energy trapping.

DOI: 10.1103/PhysRevApplied.23.044005

I. INTRODUCTION

Topological insulators behave as insulating states in the bulk but as conducting states along the edges [1]. One of the remarkable features of topological insulators is the bulk-edge correspondence, where the d-dimensional (dD) topological insulators support $(d-1)$ D gapless states at the geometric boundaries [2–4] or interfaces [5–7] formed by two distinct topological phases. Recently, realizing acoustic topological insulators in the platform of a sonic crystal has attracted increasing intention, due to the flexible controllability of the structural parameters on the macroscopic scale. To date, acoustic analogs of several kinds of topological insulators have been achieved according to distinct physical mechanisms, including the quantum Hall effect [2], the quantum spin Hall effect [5,7,8], and the quantum valley Hall effect [6,9–11], and topologically protected sound transporters are observed that are robust against defects.

Recently, by gapping out the boundary states, the concept of higher-order topological insulators has been proposed [12]. Generally, a dD nth-order topological insulator hosts $(d-n)$D boundary state, i.e., the topological state with dimensionality is two or more lower than that of the bulk, such as the hinge [13–17] or corner states [18–21]. Then, the term higher-order topological insulator has been extended to the classical acoustic system [22–26], where several typical types for creating higher-order topological states are revealed. Besides the schemes of the Jackiw-Rebbi mechanism [24,27] and quantized multipole momentum [28,29], crystalline symmetries have been utilized [30,31] in the design with sonic crystals. Changing the crystalline symmetries will cause the gapped edge or surface states [32,33], and hierarchical topological states will emerge in this gap. In C_n-rotational symmetric sonic crystals, Wannier-type higher-order topological insulators, characterized by quantized bulk polarization (namely, the Wannier center), are constructed [20,22,23,34–43]. For example, the acoustic zero-dimensional (0D) corner states are demonstrated in two-dimensional (2D) and three-dimensional (3D) topological insulators with various lattice symmetries, such as acoustic kagome lattices with C_3 symmetry [22,23,38], square lattices with C_4 symmetry [39,40], honeycomb lattices with C_6 symmetry [36,41], and a pyrochlore lattice with C_3 and generalized chiral symmetries [37]. The crystalline symmetries can force the higher-order topological states to be located at specific

*Contact author: zggeng@zjnu.edu.cn
†Contact author: xfzhu@hust.edu.cn

hinges or corners. Essentially, the rotationally symmetric lattices, featuring alternating intercell and intracell couplings, belong to the 2D [22,23,38–40] and 3D [35,37] extensions of the one-dimensional (1D) Su-Schrieffer-Heeger (SSH) mode, the domain walls of which can support the corner states when cutting through the Wannier centers. However, the prevailing Wannier-type higher-order topological insulators in original C_n-rotationally symmetric sonic crystals only host corner states within one band gap, limiting applications on multiband sound manipulations. Thus, it is necessary to explore multiple corner states in different band gaps for higher-order topological insulators, which can provide more possibilities for localizing acoustic modes and may facilitate the design of multiband acoustic sensors, acoustic isolators, and energy-trapping devices.

To obtain doubled topological boundary states, several major ways have been utilized. One is to introduce additional higher-order acoustic modes [9,44–46], which have been combined with the method of topology optimization [45], and another is to create the square-root lattice by adding additional resonators between all the original site resonators [47–49]. Besides, the hybrid-order topological insulator, which possesses the 1D gapless edge states and 0D corner states in distinct bulk gaps, is constructed either by a layer-stacking strategy [50] or by non-Hermiticity [51]. Naturally, we wonder whether we can directly design a Wannier-type higher-order topological insulator supporting multiband hierarchical topological states without a complicated physical mechanism but can realize diverse field localizations.

Inspired by the chiral symmetry of the isotropic 2D SSH model, here we construct the C_{4v}-symmetric composite lattice, i.e., an extension of the 2D SSH model [52], through simple lattice hybridization to obtain paired hierarchical topological states in two bulk gaps. By exchanging the alternating coupling strengths of the composite lattice, topologically distinct phases can be obtained, which are characterized by Wannier centers. When the Wannier centers are at the inserted sites, we can truncate the lattice into distinct nontrivial boundaries, supporting the diverse localized states within two bulk gaps. We experimentally demonstrate the higher-order topological phenomena relying on two square-shaped sonic crystals with distinct edges, where the hierarchical topological states (involving corner states, dimerlike edge states, and trimerlike edge states) are observed at both the lower and upper frequencies, termed dual-band localized topological states. Additionally, we measure the phase distributions in adjacent boundary cavities to confirm the in-phase and antiphase profiles of these boundary states, which are located in the lower and upper band gaps, respectively. Finally, by introducing perturbations at irrelevant bulk regions of the finite sonic crystals, we experimentally clarify the robustness of the localized topological states. Our work extends the scheme to construct dual-band higher-order topological states, with promising applications for designing multiband acoustic devices.

II. MODEL AND ACOUSTIC REALIZATION

We start to construct the C_{4v}-symmetric lattice from the typical 2D SSH model by inserting extra sites (purple balls) into each inversion center of the four adjacent unit cells (green balls) of the 2D SSH model. As depicted in the right panel of Fig. 1(a), the created lattice is equal to the composite lattice of the original 2D SSH model, and thus, consists of five lattice sites per unit cell, four of which (B, C, D, and E) belong to the original ones in the 2D SSH model and the remaining site (A) is viewed as the inserted one. Two primitive vectors, as denoted by red arrows in Fig. 1(a), are $\mathbf{a}_1 = (a, 0)$ and $\mathbf{a}_2 = (0, a)$, with a being the lattice constant. It should be mentioned that there are two sets of nearest-neighbor couplings, depicted by coupling strengths t_1 and t_2. Compared with the original 2D SSH lattice, site A in the composite lattice provides a route to diversify the couplings between lattice sites, around which four identical t_2 coupling interactions are established. According to the nearest-neighbor interactions in the composite lattice in Fig. 1(a), we can obtain the momentum space Hamiltonian $H(\mathbf{k})$ as

$$H(\mathbf{k}) = \begin{pmatrix} 0 & t_2 & t_2 e^{i\mathbf{k}\cdot\mathbf{a}_1} & t_2 e^{i\mathbf{k}\cdot(\mathbf{a}_1+\mathbf{a}_2)} & t_2 e^{i\mathbf{k}\cdot\mathbf{a}_2} \\ t_2 & 0 & t_1 & 0 & t_1 \\ t_2 e^{-i\mathbf{k}\cdot\mathbf{a}_1} & t_1 & 0 & t_1 & 0 \\ t_2 e^{-i\mathbf{k}\cdot(\mathbf{a}_1+\mathbf{a}_2)} & 0 & t_1 & 0 & t_1 \\ t_2 e^{-i\mathbf{k}\cdot\mathbf{a}_2} & t_1 & 0 & t_1 & 0 \end{pmatrix}, \tag{1}$$

with $\mathbf{k} = (k_x, k_y)$ being the Bloch wave vector.

Furthermore, we implement the composite-lattice model using acoustic coupling structures, shown schematically in Fig. 1(b), where the cylindrical acoustic cavities and connected tubes play the roles of sites and couplings in the tight-binding model, respectively. The hollow structure can encapsulate the air region (with a density of 1.29 kg/m^3 and speed of sound of 343 m/s) in which the acoustic waves propagate. In the design, the lattice constant, a, is 138 mm. The height and radius of each cylindrical cavity are set as $H = 60$ mm and $R = 13.8$ mm, respectively. Each pair of nearest-neighbor cavities, with a distance $L = 57.2$ mm between them, is connected by coupling tubes. The coupling strength is adjustable by varying the radius of the connecting tubes, wherein different radii indicated by r_1 and r_2 in Fig. 1(b) correspond to different coupling strengths t_1 and t_2, respectively. Since we focus on the case of the resonant acoustic dipole mode, the coupling tubes are placed at a height of $H/4$ from either the top or bottom of each cavity. In Fig. 1(c), we show the

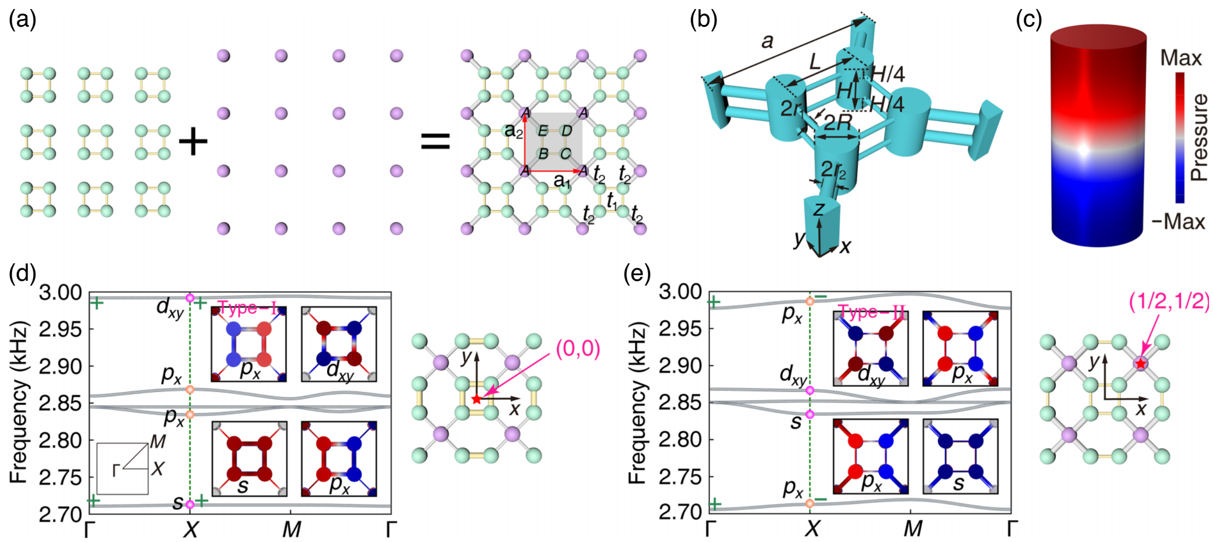

FIG. 1. (a) Schematic of the relationship between the original 2D SSH model and the C_{4v}-symmetric composite lattice. Unit cell, indicated by the transparent gray zone, consists of five sites: A, B, C, D, and E. (b) Unit cell of the sonic crystal in the air region. (c) Acoustic first-order resonant modes in a single cavity at 2858.3 Hz. (d) Bulk bands obtained by numerical simulation for the type-I unit cell with $r_1 = 4$, $r_2 = 1.3$ mm. (e) Bulk bands obtained by numerical simulation for the type-II unit cell with $r_1 = 1.3$, $r_2 = 4$ mm. In (d) and (e), the insets show the pressure-distribution profiles at the X point of the Brillouin zone for the unit cells with trivial (d) and nontrivial (e) couplings.

sound pressure in the dipole mode for the single cavity at $f_0 = 2858.3$ Hz, which varies sinusoidally along the z direction of the cavity.

To investigate the topological features, we present the simulated bulk bands for the unit cells under different coupling parameters, with a total of five bands in each case, as shown in Figs. 1(d) and 1(e). Specifically, when increasing r_1 to 4 mm and decreasing r_2 to 1.3 mm (termed a type-I unit cell), we find that two omnidirectional bulk gaps appear in Fig. 1(d), ranging from 2712 to 2834 Hz and from 2869 to 2992 Hz. The pressure distributions involved in the bands are shown in the insets of Fig. 1(d), where the selected eigenmodes at the X point on the first and second bands correspond to the s and p_x modes, and the ones on the fourth and fifth bands at the X point correspond to the p_x and d_{xy} modes. With the values of r_1 and r_2 exchanged (i.e., the type-II unit cell with $r_1 = 1.3$ and $r_2 = 4$ mm), the bulk bands of the unit cell are simulated as shown in Fig. 1(e), showing lower and upper bulk gaps spanning from 2719 to 2835 Hz and from 2868 to 2977 Hz, respectively. It is observed that the bulk bands in Figs. 1(d) and 1(e) for the two cases are different, because the composite lattices with exchanged coupling tubes cannot coincide in real space by a simple translation, unlike the 2D SSH model. In addition, we see that the selected eigenmodes on the bands at the X point take a reversed band order, either for the modes around the lower band gap or for the modes around the upper band gap. Specifically, the frequencies of the s (p_x) mode are higher than that of $p_x(d_{xy})$, located above and below the first (second) band gap, which indicates band inversion [53] in comparison with the ones in Fig. 1(d).

The presence of band inversion generally indicates the topological phase transition. To characterize the topological properties of different unit cells, we use the 2D polarization, $\mathbf{P}$, namely, the 2D Zak phase $\mathbf{Z}(\mathbf{Z} = 2\pi\mathbf{P})$, which can be given by the following expression: [54]

$$\mathbf{P} = -\frac{1}{(2\pi)^2}\iint dk_x dk_y Tr[\mathbf{A}_n(k_x\,, k_y\,)], \tag{2}$$

where $\mathbf{A}_n(k_x\,, k_y) = iu_n(\mathbf{k})|\partial_{\mathbf{k}}|u_n(\mathbf{k})$, with $|u_n(\mathbf{k})$ being the Bloch function of the nth band, and the integration is over the first Brillouin zone. It should be mentioned that the inversion symmetry for the C_{4v}-symmetric composite lattice puts a strong constraint on the values of $\mathbf{P}$, which can be determined by analyzing the symmetries (i.e., parities) of the eigenmodes at specific Γ and X points:

$$P_i = \frac{1}{2}\left(\sum_n q_i^n \text{modulo2}\right), (-1)^{q_i^n} = \frac{\eta_n(X_i)}{\eta_n(\Gamma)}, \tag{3}$$

where i denotes x or y, and $P_x = P_y$ due to the C_{4v} symmetry of the composite lattices. η_n stands for the parity under π rotation of the eigenmode for the nth band at the symmetry point, where monopolar, s, and quadrupolar, d_{xy}, modes have even parity (+), while dipolar, p, modes have odd parity (−). $\sum_n q_i^n$ denotes the summation of q_i^n for all bands below the target band gap. Following this principle, we analyze the eigenmodes for both $r_1 > r_2$ and $r_1 < r_2$

to check the parities at the Γ and X points on the bulk bands, as shown in Figs. 1(d) and 1(e), Specifically, two isolated bulk bands, i.e., the first and fifth bands, for a type-I unit cell possess the same parity [see Fig. 1(d)] at these points, whereas the ones for a type-II unit cell possess opposite parities [see Fig. 1(e)]. Accordingly, similar to the isotropic 2D SSH model, for the first and second objective bulk gaps, we obtain $\mathbf{P} = (0, 0)$ for the type-I unit cell and $\mathbf{P} = (1/2, 1/2)$ for the type-II unit cell, indicating that the two unit cells belong to different topological phases. These topological phases cannot be adiabatically transformed from one to the other without closing the band gaps or breaking the symmetries. Essentially, the composite square lattice is the extension of the isotropic 2D SSH model, which possesses doubled nontrivial bulk gaps. We discuss the origin of doubled band gaps, as well as the nontrivial topological properties based on the 2D SSH model, in Appendix A.

Furthermore, according to the polarization values, we can obtain the positions of Wannier centers in two distinct unit cells, since the bulk polarizations can indicate the deviation of the Wannier center (i.e., the average position of the eigenstates of the dispersion bands) from the center of the sites in the unit cell. As can be seen from the right panels of Figs. 1(d) and 1(e), the type-I unit cell holds its Wannier center at the origin $(0, 0)$ of the unit cell, whereas for the type-II unit cell the Wannier center lies at $(1/2, 1/2)$. We want to emphasize that spatial inversion symmetry in the composite lattice restricts the Wannier center to two positions, i.e., at the center and the corner of the unit cells, corresponding to the topologically trivial and nontrivial phases, respectively. According to previous studies [22,23,35,38], when the finite lattice cuts through the Wannier centers, the presence of corner states can be expected at the corners as well as the topological edge states along the edges. Thus, the unit cell with nonzero bulk polarization, i.e., nontrivial coupling, can serve as a good foundation for designing hierarchical higher-order topological states on the composite square lattice.

To explore the potential second-order corner states in the composite sonic crystals, we construct a square-shaped lattice with 89 sites enclosed by nontrivial edges, where a series of Wannier centers are positioned on the edges, as indicated by red stars on blue dashed lines in Fig. 2(a). To check the dependence of the emergence of higher-order topological states upon varying the coupling ratio, t_1/t_2, additional eigenfrequency spectra for the finite lattice are shown in Fig. 2(b), where we see two groups of in-gap states in distinct bulk gaps for $t_1/t_2 < 1$, while they vanish for $t_1/t_2 > 1$. Note that $t_1/t_2 = 1$ corresponds to the occurrence of the topological phase transition at this point. By selecting a fixed value of $t_1/t_2 = 0.115$ [marked by the green dashed line in Fig. 2(b)], which can be well matched to the parameters of the type-II unit cell with $r_1 = 1.3$

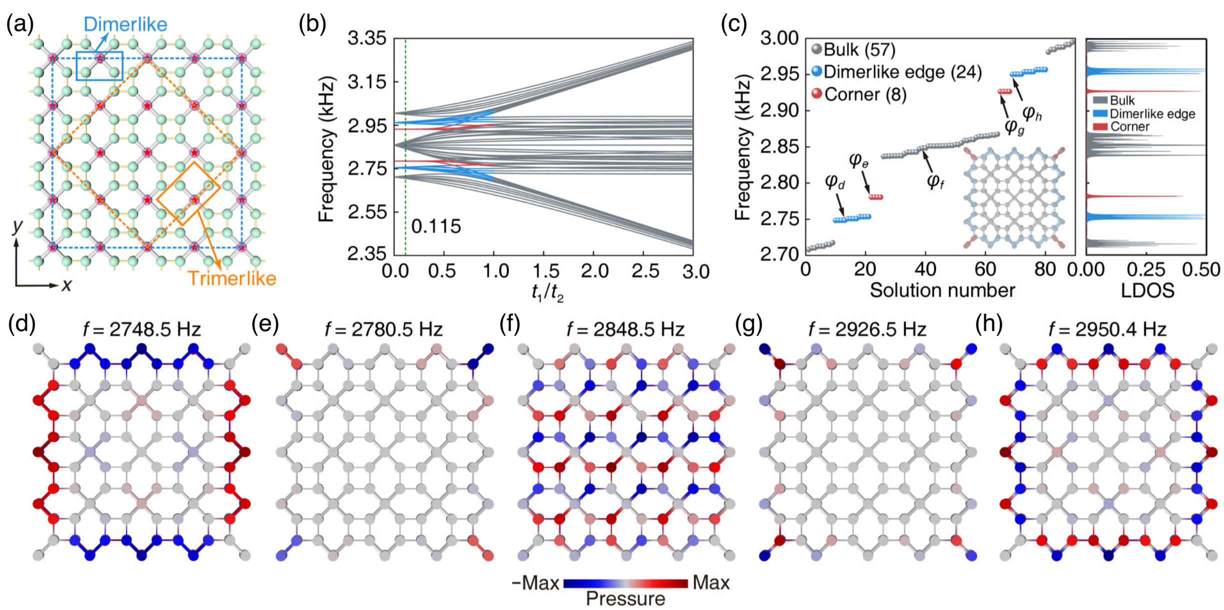

FIG. 2. (a) Lattice schematic of the nontrivial topological phase, where the Wannier centers are labeled by red stars. Blue and orange dashed lines indicate the truncated edges of two square-shaped lattices, with horizontal and slant boundaries relative to the x axis, respectively. (b) Eigenfrequency spectra of the horizontally oriented lattice with 89 sites in (a) as a function of the parameter t_1/t_2. Gray, blue, and red lines represent the bulk states, dimerlike edge states, and corner states, respectively. (c) Eigenfrequencies and relevant local density of states for the finite acoustic lattice with $r_1 = 1.3$ and $r_2 = 4$ mm. Colored cavities in the inset are utilized to obtain the local density of states for different modes. (d)–(h) Eigenpressure distributions of φ_d, φ_e, φ_f, φ_g, and φ_h modes [marked in (c)].

and $r_2 = 4$ mm, in Fig. 2(c) we give the numerically simulated eigenfrequencies and relevant local density of states (frequency-response spectra) of the finite sonic crystal. As expected, the in-gap edge and corner states coexist in both the lower and upper bulk gaps, as verified by the local density of states shown in the right panel. Within one bulk gap, there are 12 dimerlike edge states (blue colored) and four corner states (red colored). Here, the corner states can be found at frequencies of 2780 and 2927 Hz, while the dimerlike edge states exist at the frequencies of 2748, 2751, and 2753 Hz in the lower bulk gap and 2950, 2954, and 2957 Hz in the upper bulk gap, both for the eigenfrequencies and the frequency-response spectra shown in Fig. 2(c). In contrast, the lattice with swapped values of r_1 and r_2 fails to support multiple topological boundary states, because in the phase of $t_1/t_2 > 1$ the Wannier centers are shifted to the interior of the horizontal-boundary lattice shown in Fig. 2(a).

Next, we display the eigenpressure distributions of the φ_d, φ_e, φ_f, φ_g, and φ_h modes [marked by black arrows in Fig. 2(c)] in Figs. 2(d)–2(h), respectively. It is evident that topological dimerlike edge states [see Figs. 2(d) and 2(h)] and corner states [see Figs. 2(e) and 2(g)] are localized on the nontrivial edges and corners, respectively, showing the dual-band hierarchical topological states in a composite acoustic crystal. According to the above eigenfrequencies and relevant mode distributions, we find that the number of acoustic corner modes in two bulk gaps is equal to the number of sites at four corners, indicating that the inserted sites, terminated by the Wannier centers, can induce additional corner states. In addition, we notice that the phase profiles of the boundary states shown in Figs. 2(d) and 2(e) remain an in-phase characteristic, whereas those in Figs. 2(g) and 2(h) exhibit an antiphase characteristic. This behavior is revealed by the eigenpressure distributions of the nearest-neighbor boundary sites. It should be noted that, in the truncated tight-binding model (with $t_1/t_2 = 0.115$), the in-phase and antiphase mode distributions for the topological eigenstates in the lower and upper band gaps, respectively, also exist. Further details are provided in Appendix B. Here, the phase difference of the boundary modes can be attributed to the constraint imposed by spatial inversion symmetry of the composite lattices [52], analogous to the case in a typical isotropic 2D SSH model (see Appendix A).

Unlike the localized edge and corner modes, the bulk state in the middle band at 2848.5 Hz, shown in Fig. 2(f), is distributed over nearly the entire lattice, exhibiting some spatial overlap with the lattice edges. In contrast, the bulk states in the lower and upper bands, located within the interior region of the lattice, have negligible spatial overlap (the lower and upper bulk states are not explicitly shown).

III. EXPERIMENTAL DEMONSTRATION OF HIGHER-ORDER TOPOLOGICAL PHENOMENA

Based on the above simulation results, an experimental sample consisting of hollow epoxy resin cylinders was fabricated by 3D printing technology, as shown in the left panel of Fig. 3(a). It is identical to the parameter used in Fig. 2(c); the inner height and radius of the cylindrical cavity sample are 60 and 13.8 mm, respectively, and the length of the connecting tubes is 29.6 mm. Note that three types of pump-probe configurations targeting the bulk, edge, and corner regions [marked by colored dots in Fig. 3(a)] are used to detect the frequency-response spectra. In the right panel of Fig. 3(a), we show the experimental setup. In the experiment, the sample was anchored on the optical platform holder, and a pointlike speaker (Knowles ED-23814), stimulated by the signal generator (RIGOL DG1032Z), was positioned at the cylindrical cavities after removing the appendant source cap. The acoustic pressure amplitudes on the upper surfaces of cylindrical cavities were extracted by inserting a 1/4-inch microphone (GRAS 46BD) into the perforated measuring holes. The unscanned holes were plugged to prevent sound leakage. All data were recorded and analyzed with an NI Compact-cDAQ-9185 four channel analyzer, in which the frequency response was received by performing fast Fourier transform analysis with SignalPad software.

To verify the specific characteristics of the bulk, edge, and corner states, we first measure the transmission spectra from the cavities marked by colored dots in Fig. 3(a). For the process, the exciting and measuring of sound signals proceed in the same cavity for each response spectrum. The results of measured transmissions, with a frequency interval of 1 Hz, are shown as gray, red, and blue curves in Fig. 3(b), corresponding to the bulk, corner, and dimerlike edge modes, respectively. Within the two bulk gaps, four resonant peaks are observed for the dimerlike edge mode and corner mode. Specifically, two blue ones correspond to the dimerlike edge states around frequencies of 2767.5 and 2973.5 Hz, and two red ones correspond to the corner states around frequencies of 2805.5 and 2954.5 Hz. The measured spectra can capture the features of the calculated results in Fig. 2(c), where the frequency deviations may be due to the thermoviscous damping effect in narrow structural channels and the fabrication error of the sample. The lower peaks for the corner and dimerlike modes in the first bulk gap on the response curves can be attributed to slight structural differences at the positions of the source and the microphone (i.e., detector) due to the fabrication errors in 3D printing, causing different viscous absorptions in the sample material.

Furthermore, to confirm the emergence of topological edge and corner states, we map the distributions of the pressure field by exciting each cavity and detecting the amplitude response of sound pressure in the same cavity.

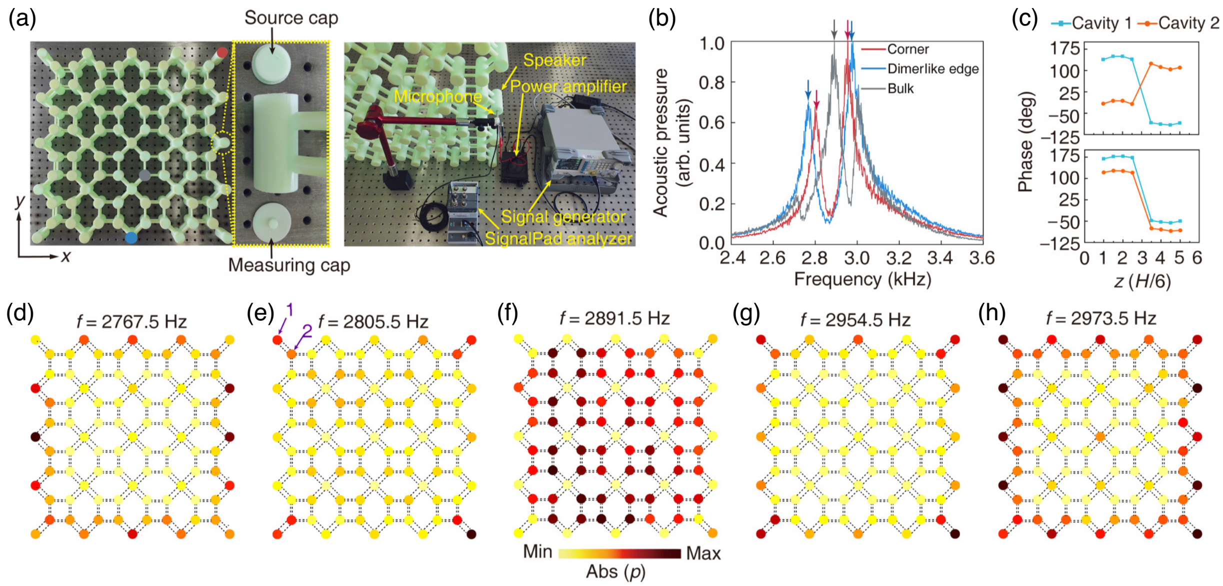

FIG. 3. (a) Photograph of the fabricated acoustic sample and the experimental setup. Enlarged view shows the design of the acoustic cavity for measurement. (b) Measured transmission spectra at different regions of the sample marked in (a). (c) Measured phase distributions along the z direction in the two adjacent corner cavities [labeled 1 and 2 in (e)] for the corner states at 2805.5 (lower panel) and 2954.5 Hz (upper panel). (d)–(h) Measured acoustic amplitude distributions for the dimerlike edge states [(d),(h)], corner states [(e),(g)], and bulk states (f).

With such a method, the field distributions are measured by setting the excitation frequencies at the resonant frequencies [indicated by arrows in Fig. 3(b)]. From the measured acoustic amplitude fields shown in Figs. 3(d)–3(h), one can directly recognize the wave patterns of the corner states, dimerlike edge states, and bulk states. For instance, when operating at the corner resonant frequencies, the pressure responses at the four corners, as shown in Figs. 3(e) and 3(g), are much higher than those at other points of the lattice, demonstrating the key feature of corner states. Note that the slight spatial overlaps of the corner and dimerlike edge states at higher frequencies [shown in Figs. 3(g) and 3(h)] can be attributed to the smaller frequency interval (about 19 Hz) between them in comparison with the ones at lower frequencies (about 38 Hz). To observe the phase difference of topological corner states in different bulk gaps, we measure the phase distributions along the z direction in the two corner cavities [labeled 1 and 2 in Fig. 3(e)], with the sound source fixed in corner cavity 1. As shown in Fig. 3(c), we can obviously find the in-phase and antiphase features for the two corner states at frequencies of 2805.5 and 2954.5 Hz, respectively. These undoubtedly demonstrate the emergence of dual-band second-order topological states in the square-shaped composite sonic crystal. To reveal sound attenuation in the experiment, we also measure the field distributions at resonant frequencies by sequentially fixing the sound source at the relevant edge, corner, and bulk cavities, as detailed in Appendix C.

The square-shaped lattice mentioned above has only one type of dimerlike edge. Relying on the parameters used in the above sample, i.e., $r_1 = 1.3$ and $r_2 = 4$ mm, in Fig. 4(a) we construct an additional square-shaped sample with 53 acoustic cavities, which contains four trimerlike edges and four dimerlike edges. Note that in this sample the dimerlike edge is dimensionally equivalent to a corner. The lattice can be regarded as being truncated from the periodic lattice along the orange dashed lines shown in Fig. 2(a). According to the positions of Wannier centers, we expect two kinds of edge states on the lattice boundaries. The numerically simulated eigenfrequencies in Fig. 4(b) show that both the fourfold degenerate dimerlike edge states (which dimensionally serve as corner states) and the quasi-fourfold-degenerate trimerlike edge states simultaneously reside within the lower and upper bulk gaps. For the mode distributions, as shown in the insets of Fig. 4(b), the eigenpressure fields at 2729.7 and 2973 Hz are located at the trimerlike edges, while those at 2751 and 2953.5 Hz are located at the dimerlike edges. The experimental measurements are based on the same protocol as that described in the paragraphs above and can match well with numerical predictions. From the measured frequency-response spectra in Fig. 4(c), we can observe that four resonant peaks appear within two bulk gaps, where two orange arrows indicate the peaks of trimerlike edge states at 2756.5 and 3006.5 Hz, and two blue arrows indicate the peaks of dimerlike edge states at 2775.5 and 2975.5 Hz. Another gray peak at 2900.5 Hz, which

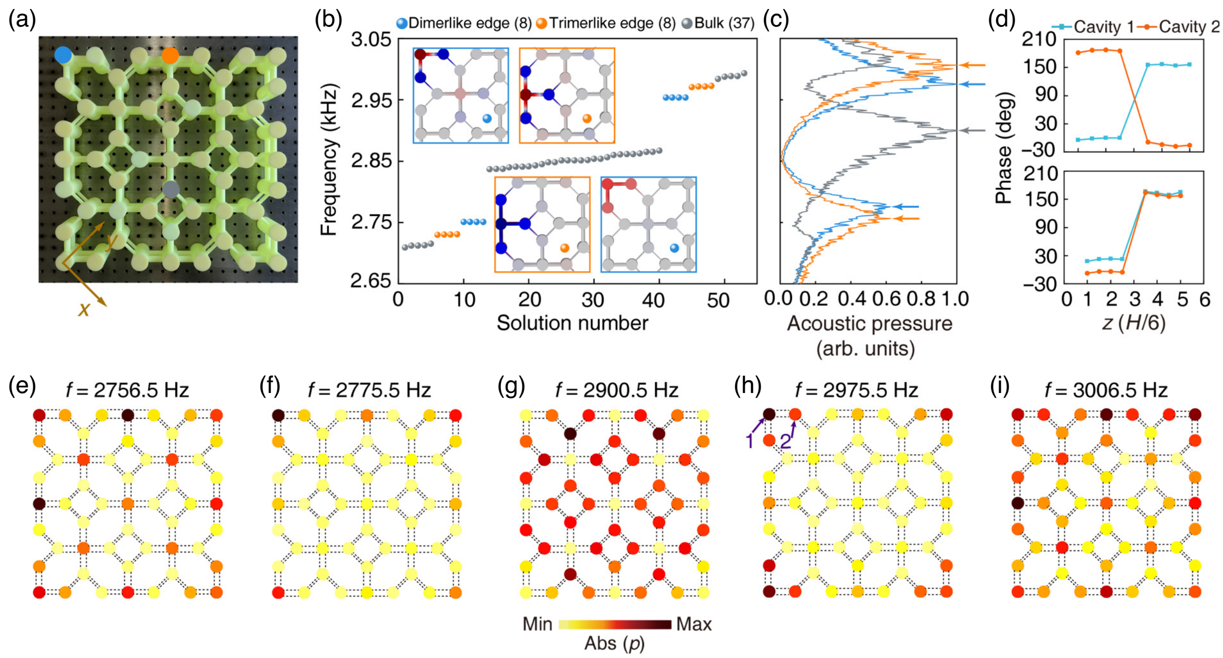

FIG. 4. (a) Photograph of the sample containing four trimerlike edges and four dimerlike edges, where colored dots indicate the positions to detect the frequency responses. (b) Numerically simulated eigenfrequencies of the same finite lattice as in (a). Bottom (top) insets, eigenpressure distributions of the trimerlike and dimerlike edges states at frequencies of 2729.7 and 2751 Hz (2973 and 2953.5 Hz), respectively. (c) Measured response spectra of the bulk (gray), dimerlike edge (blue), and trimerlike edge (blue) states. (d) Measured phase distributions along the z direction in the two adjacent boundary cavities [labeled 1 and 2 in (h)] for the dimerlike states at 2775.5 (lower panel) and 2975.5 Hz (upper panel). Measured acoustic amplitude distributions for the bulk (g) state, trimerlike edge [(e),(i)] states, and dimerlike edge [(f),(h)] states.

separates the edge states into two groups, results from the bulk state.

Next, we measure the field patterns of these states by using the peak frequencies as the excitation frequencies. As seen in Figs. 4(e)–4(i), the relevant acoustic amplitude distributions at the trimerlike edges [Figs. 4(e) and 4(i)], dimerlike edges [Figs. 4(f) and 4(h)], and bulk region [Fig. 4(g)] are significantly higher than those at other points in the lattice. For the trimerlike edge states, due to the small frequency intervals of both the bulk modes and the dimerlike edge modes, there is some spatial overlap with the bulk region and the dimerlike edges. Similarly, to reveal the phase difference for the in-gap states, we measure the phase distributions along the z direction in two boundary cavities [labeled 1 and 2 in Fig. 4(h)] for the dimerlike edge states. As shown in the lower and upper panels of Fig. 4(d), the phase profiles of the dimerlike edge states remain in phase at the lower frequency and antiphase at the upper frequency. Thus, we demonstrate the diverse (trimerlike and dimerlike) topological edge states in doubled bulk gaps, depending on the truncated composite lattice with nontrivial edges. In addition, these edge states can be transferred to adjacent dimerlike edges by transforming the square-shaped lattice [shown in Fig. 4(a)] into topologically distinct phases with $r_1 = 4$, $r_2 = 1.3$ mm, as detailed in Appendix D. To investigate the influence of boundary shape on the emergence of topological boundary states, we discuss the eigenfrequencies of finite lattices with different boundaries in Appendix E.

In the following, we again select the two truncated sonic crystals [as used in Figs. 3(a) and 4(a)] to investigate the robustness of topological boundary states, including corner states and dimerlike edge states. For the composite lattices with inversion symmetry, perturbations will not be capable of having a significant impact on these located states, as long as the parity alternation at the Γ and X points of the Brillouin zone is preserved [52]. To reveal the effect of topological protection, we intentionally introduce perturbations into the interior bulk regions as bulk disorder, as illustrated by the light-green regions in Figs. 5(a) and 5(b). Here, the perturbations (defects) are mimicked by introducing small solid cylinders [shown by the magnified illustrations in Figs. 5(a) and 5(b)] with $R_d = 6$ mm and height, H_d, uniformly distributed from 1 to 3 mm. These cylinders, which are added to the bottom of these cavities, can serve as the additional random onsite potential energies to induce small resonant frequency shifts. Thus, the resonant frequencies of the disordered acoustic cavities should be set as $f_0(1 + df_i)$, where f_0 is the original resonant frequency, and df_i represent a series of

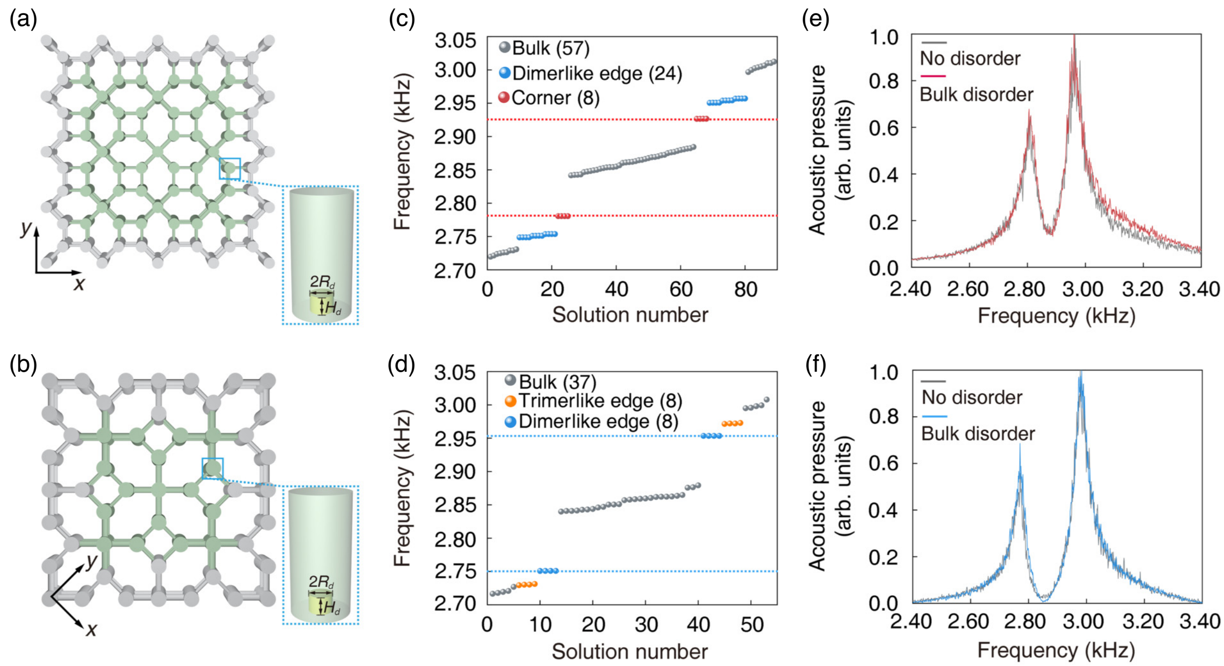

FIG. 5. (a),(b) Schematics of bulk disordered sonic crystals, as indicated by the light-green regions. Insets show closer views of the embedded solid cylinders (yellow columns) in the cavities. (c),(d) Simulated eigenfrequencies for the bulk disordered sonic crystals shown in (a),(b), respectively. Two red (blue) dashed lines indicate the corner (dimerlike edge) mode frequencies for the lattice without any disorder. Measured spectra at one corner (e) and at one dimerlike edge (f) in different sonic crystals with bulk disorder. Gray lines correspond to the case of no disorder.

random numbers equally distributed from $-\delta$ to δ. Here, i denotes the site index and δ is a parameter of disorder strength. From the calculated eigenfrequencies shown in Figs. 5(c) and 5(d), we can observe that the bulk states are shifted to higher frequencies, while these localized boundary states within two bulk gaps all have the same eigenfrequency as those in the unperturbed sonic crystals. Thus, the main features of dual-band hierarchical topological states remain unchanged, because these states exist stably in the two bulk spectral gaps.

To verify the above results, we fabricate small epoxy resin rods, the parameters of which are the same as those used in simulations, and then embed them into the experimental cavity samples. Under bulk disorder, the measured response spectra for the corner and dimerlike edge cavities [red and blue curves in Figs. 5(e) and 5(f), respectively] exhibit resonant peaks at 2805.5 and 2960.5 Hz for the corner states, and at 2770.5 and 2983.5 Hz for the dimerlike edge states, which nearly overlap with those observed in the absence of disorder.

Thus, we conclude that the localized boundary states are robust against bulk disorder, both at the lower frequency and at the upper frequency. For comparison, by introducing random disorder into the corner and dimerlike edge regions in two distinct sonic crystals, we find that the response peaks always survive but are shifted to higher frequencies, as discussed in Appendix F. In fact, the hierarchical topological states essentially depend on the local configurations of the boundaries, thus the disorder at irrelevant regions cannot affect the response frequencies of the localized states; this is investigated in Appendix G. Finally, according to the disorder strength parameter, δ, we assess the thresholds of bulk and corner disorders, as displayed in Appendix H.

IV. CONCLUSIONS

We have realized an acoustic dual-band higher-order topological insulator based on a composite sonic crystal with C_{4v} symmetry, which is constructed by adding extra sites into each inversion center of four adjacent unit cells in the original 2D SSH model. The distinct topological phases of sonic crystals can be characterized by bulk polarizations, which can be revealed by the parity features of different high-symmetry points due to the inversion symmetry of the composite lattice. By virtue of the inserted sites, diverse boundaries with nontrivial couplings are obtained in different square-shaped sonic crystals, where the Wannier centers pass through the truncated edges. In the topologically nontrivial phase, the doubled acoustic hierarchical topological states with diverse acoustic localizations are experimentally observed in two distinct bulk gaps, as evidenced by both the frequency response spectra and the field distributions of different acoustic modes.

Compared to a typical 2D SSH model, which only has one group of corner states, the inserted sites in the composite lattices can induce additional corner states as well as diversified dimerlike and trimerlike edge states in two bulk gaps. To distinguish different localized states, we experimentally demonstrate the in-phase and antiphase profiles of these corner and dimerlike edge states by measuring the phase information of two adjacent boundary cavities along the z direction. Furthermore, based on bulk- and boundary-disordered sonic crystals, the topological robustness of corner and dimerlike edge states is verified under bulk disorder by comparing the measured frequency-response spectra with relevant boundary disorders. This work provides an efficient way to explore multiple higher-order topological states in a sonic crystal, which may contribute to the construction of multiband acoustic devices.

ACKNOWLEDGMENTS

This work was supported by the National Natural Science Foundation of China (Grants No. 12204418, No. 12474470, and No. 12404511).

DATA AVAILABILITY

The data that support the findings of this study are available from the corresponding author upon reasonable request.

APPENDIX A: HIGHER-ORDER TOPOLOGICAL PHENOMENA IN THE ISOTROPIC 2D SSH MODEL

Here, we utilize the isotropic 2D SSH model to explain the topological origin of the composite lattice [see Fig. 1(a)]. The schematic in Fig. 6(a) shows the 2D tight-binding model with alternating intracell and intercell hopping specified by t_1 and t_2 (indicated by thin yellow and thick gray sticks), respectively, which represents a 2D generalization of the SSH model. Thus, there are four lattice sites numbered from one to four in one unit cell. Under the lattice vectors $\mathbf{a}_m = (a, 0)$ and $\mathbf{a}_n = (0, a)$ (a is set to 1 for simplicity), we can derive the tight-binding Hamiltonian in $\mathbf{k}$ space for the 2D SSH model, which is written as

$$H_0(\mathbf{k}) = \begin{pmatrix} 0 & 0 & t_1 + t_2 e^{i\mathbf{k}\cdot\mathbf{a}_m} & t_1 + t_2 e^{-i\mathbf{k}\cdot\mathbf{a}_n} \\ 0 & 0 & t_1 + t_2 e^{i\mathbf{k}\cdot\mathbf{a}_n} & t_1 + t_2 e^{-i\mathbf{k}\cdot\mathbf{a}_m} \\ t_1 + t_2 e^{-i\mathbf{k}\cdot\mathbf{a}_m} & t_1 + t_2 e^{-i\mathbf{k}\cdot\mathbf{a}_n} & 0 & 0 \\ t_1 + t_2 e^{i\mathbf{k}\cdot\mathbf{a}_n} & t_1 + t_2 e^{i\mathbf{k}\cdot\mathbf{a}_m} & 0 & 0 \end{pmatrix}. \quad (A1)$$

Here, the Hamiltonian possesses chiral symmetry, i.e., $\gamma H_0(\mathbf{k})\gamma = -H_0(\mathbf{k})$, and the chiral symmetry operator, γ, is

$$\gamma = \begin{pmatrix} 1 & 0 & 0 & 0 \\ 0 & 1 & 0 & 0 \\ 0 & 0 & -1 & 0 \\ 0 & 0 & 0 & -1 \end{pmatrix}, \quad (A2)$$

where its eigenstates corresponding to eigenvalues $+1$ and -1 can reflect the phase-profile differences between paired topological states in different bulk gaps.

Correspondingly, the acoustic counterpart of the unit cell is designed as shown in the lower panel of Fig. 6(a), where the interactions between the nearest-neighbor cavities are provided by the waveguide tubes. The structural parameters of the acoustic unit cell are the same as those used in Fig. 1(b), except that the lattice constant, a_0, is changed to 114.4 mm. With values of $r_1 = 1.3$ and $r_2 = 4$ mm (i.e., $t_1 < t_2$), we expect topologically nontrivial phenomena in the acoustic system, which is operated in the strong-coupling regime. In Fig. 6(b), we show the simulated bulk bands, of which the paired bulk gaps occur as expected, ranging from 2726.3 to 2829.4 Hz and from 2859.7 to 2973.9 Hz for the lower and upper bulk gaps, respectively. Given that the higher-order topological features are only relevant to the first and the fourth bands, we focus on these eigenpressure profiles at the Γ and X points of the two isolated bands. As shown in the inset of Fig. 1(b), the s and d_{xy} modes at the Γ point exhibit even parity (+), whereas the p_x and p_y modes at the X point exhibit odd parity (−). The parity difference of different high-symmetry points is a hallmark of the nontrivial topological characteristics of the 2D SSH model. For the nontrivial coupling lattice, the polarization equals $\mathbf{P} = (1/2, 1/2)$, corresponding to the nontrivial Wannier centers located at the corners of the unit cell, as schematically illustrated in the inset of Fig. 6(b).

Then, we truncate the square-shaped lattice with nontrivial edge and corners, the eigenfrequency spectra of which in Fig. 6(c) contain paired in-gap edge states at 2775, 2780, and 2785 Hz in the lower bulk gap and at 2920, 2927, and 2932 Hz in the upper bulk gap. Besides the edge states, the degenerate corner states close to the bulk

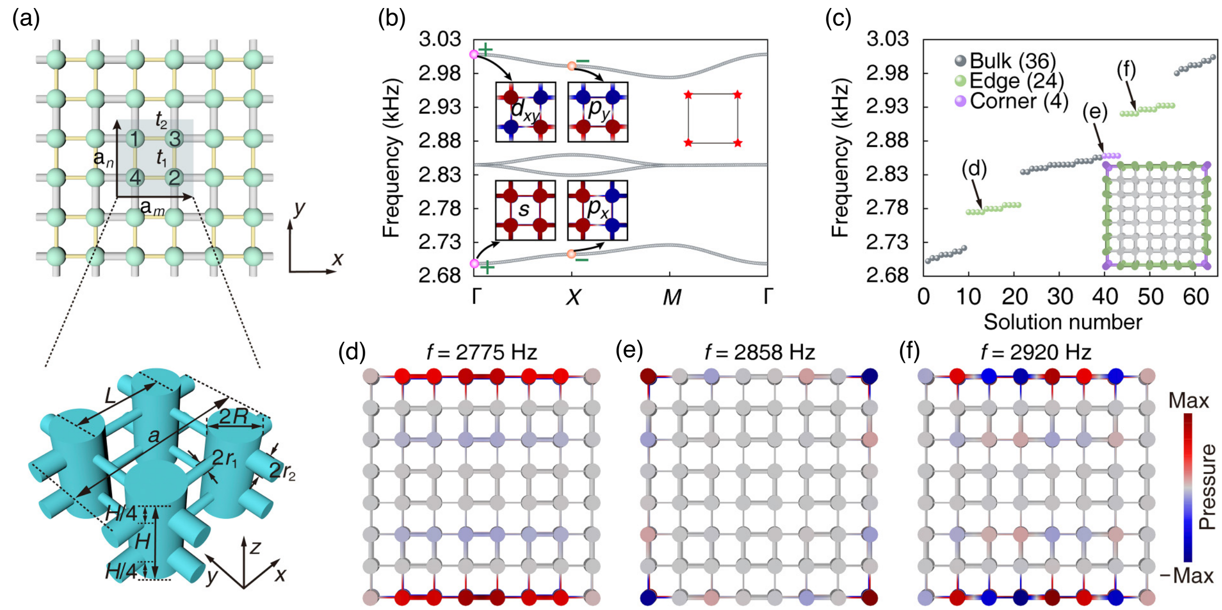

FIG. 6. (a) Schematics of the isotropic 2D SSH model and corresponding acoustic unit cell. (b) Bulk bands of the periodic structure with $r_1 = 1.3$ and $r_2 = 4$ mm. Inset, pressure-distribution profiles at Γ and X points of the Brillouin zone for the isolated bands. (c) Eigenfrequency spectra of the finite lattice with nontrivial edges (shown in the inset). Eigenpressure distributions of the in-phase edge state (d), corner state (e), and antiphase edge state (f).

ones appear at 2858 Hz. To analyze the field patterns of selected eigenstates, as indicated by the arrows in Fig. 6(c), we find that the edge [Figs. 6(d) and 6(f)] and corner states [Fig. 6(e)] are located at the nontrivial edge and corners, respectively. In particular, the edge states at the lower and upper frequencies exhibit in-phase and antiphase eigenpressure patterns, as dictated by the symmetry feature of the 2D SSH lattice. Based on the above analyses, we can regard that the topological behaviors of the paired bulk gaps and edge states in the 2D SSH lattice can be extended to the composite square lattice due to the inversion symmetries in the two lattices.

APPENDIX B: MODE DISTRIBUTIONS OF THE LOCALIZED STATES IN A TIGHT-BINDING MODEL

To further verify the phase profiles of the in-gap states, we calculate the energy eigenvalues at a fixed coupling ratio of $t_1/t_2 = 0.115$ of the square-shaped tight-binding model, as indicated by the blue dashed lines in Fig. 2(a). Clearly, in Fig. 7(a), we can see the paired corner and dimerlike edge states in two bulk gaps. The eigenfields of the φ_{e1} and φ_{c1} states in the first bulk gap, with energy values of -1.457 and -1, exhibit in-phase field patterns [see Figs. 7(b) and 7(c), respectively]. In contrast, the eigenfields of the φ_{c2} and φ_{e2} states in the second bulk gap, with energy values of 1 and 1.457, display antiphase field patterns [see Figs. 7(d) and 7(e), respectively]. Thus, for the tight-binding case, the mode-distribution features of the higher-order topological states fit well with the ones in finite acoustic crystals.

APPENDIX C: INFLUENCE OF SOUND ATTENUATION IN THE SAMPLE

For the coupled acoustic system, the narrow waveguide tubes between adjacent cavities will inevitably produce sound attenuation due to the thermoviscous damping effect. To reveal sound attenuation in the sample, we now fix the speaker at the source positions to excite the sound wave and move the microphone from one to another to detect the sound signals in all cavities. With such a method, the acoustic wave fields of the edge, corner, and bulk states are measured at their resonant frequencies, as shown in Figs. 8(a)–8(e), where the sound waves are distributed in the vicinity of the sound source, exhibiting significant attenuation. Thus, to keep with the eigenmode distributions, we map the field patterns by exciting each cavity with a speaker and measuring the acoustic wave amplitude within the same cavity [as exhibited by the results in Figs. 3(d)–3(h)] to avoid the influence of sound attenuation on the field distributions.

According to the measured results, sound dissipation in the experiment can be assessed by numerical simulation. Specifically, we modify the speed of sound as a complex number, which can be written as $c = c_{\mathrm{air}} + ic_{\prime}$, with $c_{\mathrm{air}} = 343$ m/s and $c_{\prime}$ relating to the loss. In the simulation, the sound source is placed at the same position as the experiment case to excite the sound wave

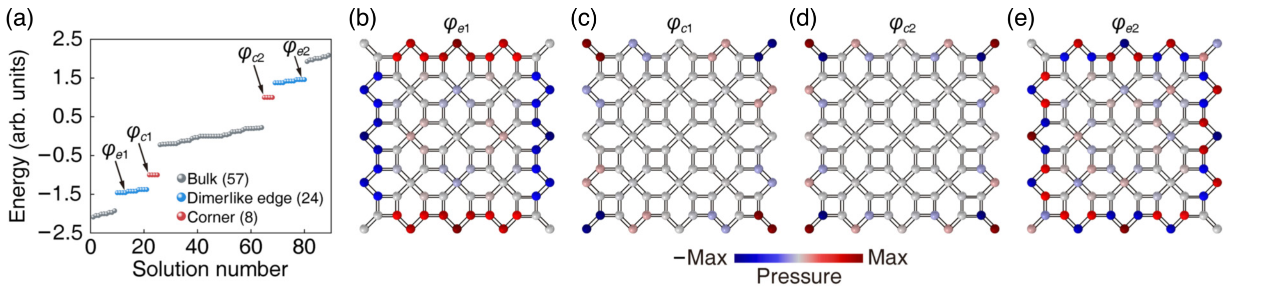

FIG. 7. (a) Energy spectra for $t_1/t_2 = 0.115$. Red and blue modes indicate corner states and dimerlike edge states, respectively. (b)–(e) Mode distributions for the in-gap states φ_{e1}, φ_{c1}, φ_{c2}, and φ_{e2}, as denoted by the arrows in (a).

at the experimental resonant frequency, under which we set $c_\prime = 8$ m/s to match the realistic loss. As shown in Figs. 8(f)–8(j), the acoustic pressure fields exhibit similar behavior to the above experimental case. Under the same excitation condition, we consider the case without sound loss ($c_\prime = 0$ m/s) in the simulation, the results of which are displayed in Figs. 8(k)–8(o). It can be found that the acoustic pressure fields corresponding to edge, corner, and bulk states are diffused into the larger lattice regions in comparison with the loss case. Thus, these field distributions reveal the existence of obvious sound attenuation in the acoustic system, which can be decreased by enlarging the cross sections of the connecting tubes.

APPENDIX D: EIGENMODES FOR A FINITE LATTICE WITH VARIED EDGES IN TOPOLOGICALLY DISTINCT PHASES

Here, we employ a square-shaped lattice with varied slant edges to investigate the decisive role of the strong coupling strength in the emergence of topological boundary states, which can directly determine the position of the Wannier center. As shown in Fig. 9(a), we exchange the coupling-strength parameters of the original lattice [shown in Fig. 4(a)], i.e., $r_1 = 4$, $r_2 = 1.3$ mm, to construct strong coupling around different types of boundary sites, such as the red-colored B, C, D, and E boundary sites in

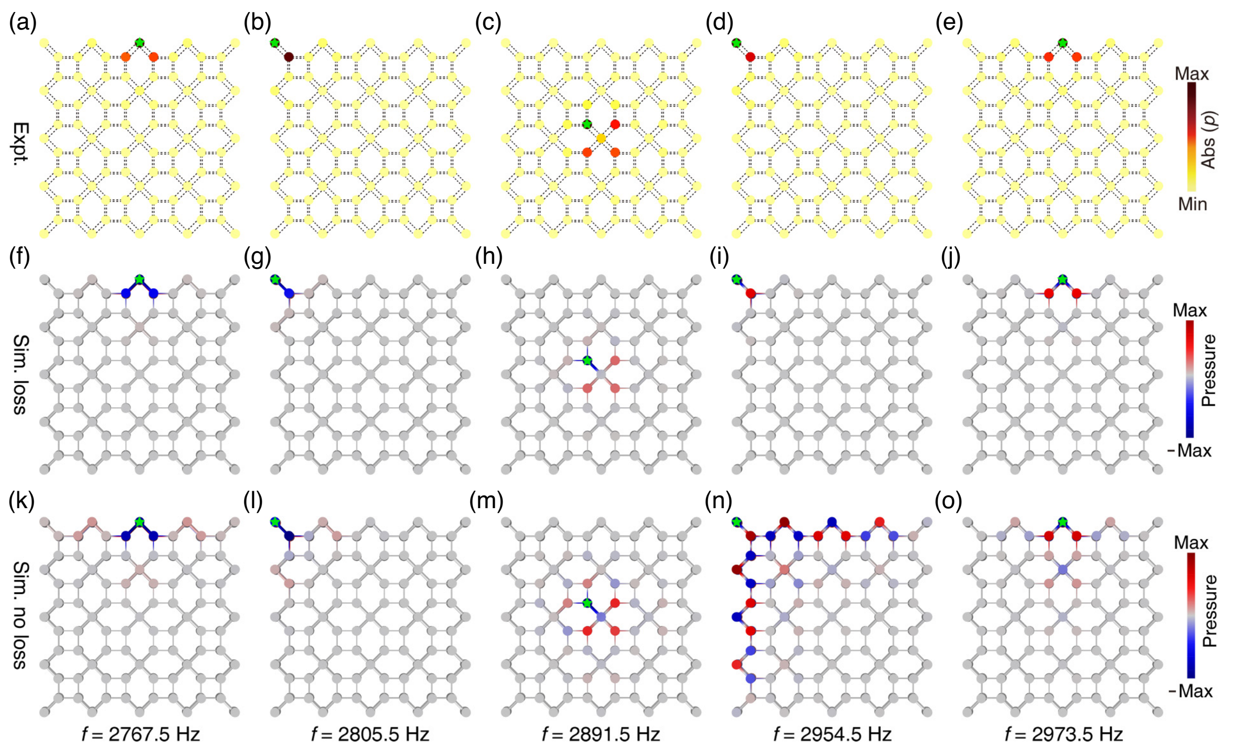

FIG. 8. (a)–(e) Measured acoustic amplitude profiles for the dimerlike edge states, corner states, and bulk states, with sound sources fixed at the corresponding positions labeled by green stars. (f)–(j) Simulated field distributions under the same excitation conditions as experiments (a)–(e) but with $c_\prime = 8$ m/s for matching the loss. (k)–(o) Simulated field distributions under the same excitation conditions as the experiments with $c_\prime = 0$ m/s.

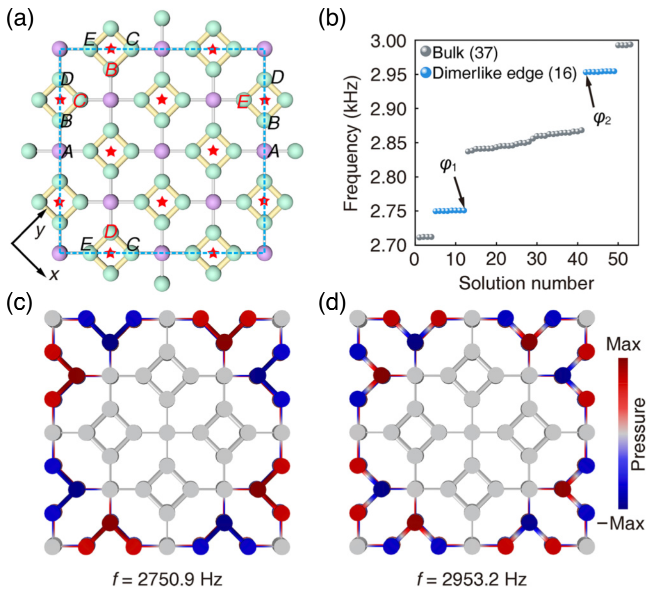

FIG. 9. (a) Schematic of the finite lattice with Wannier centers around the concave inward dimerlike edges. (b) Eigenfrequency spectra of the sonic crystal corresponding to (a) with $r_1 = 4$, $r_2 = 1.3$ mm. (c),(d) Eigenpressure distributions of the φ_1 and φ_2 states, respectively.

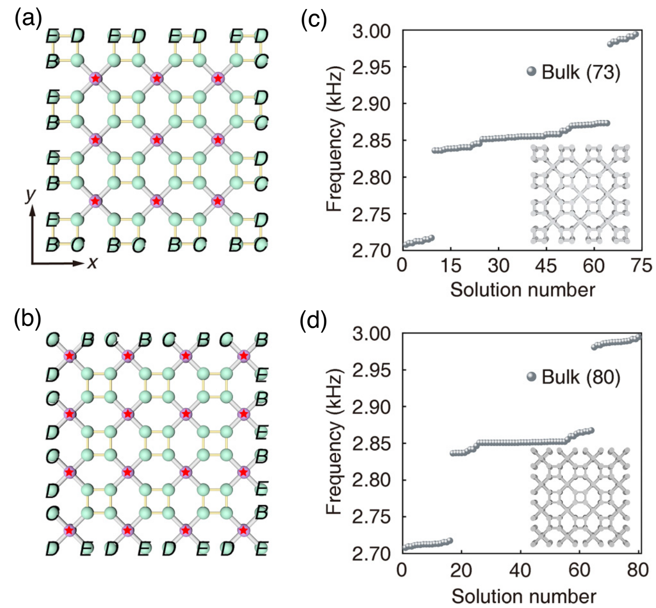

FIG. 10. (a),(b) Schematic of the truncated lattice with B, C, D, and E boundary sites in phase $t_1/t_2 < 1$. (c),(d) Eigenfrequency spectra of the acoustic lattices shown in the insets.

Fig. 9(a). The Wannier centers (marked by red stars) in Fig. 9(a) along the lattice edges can indicate the nontrivial coupling of the edges, which are concave inward in comparison with the original dimerlike edge. As verified by the eigenfrequency spectra shown in Fig. 9(b), we see that quasi-eightfold-degenerate dimerlike edge states exist in both the lower and upper bulk gaps. The eigenpressure fields of the φ_1 and φ_2 states [indicated by the arrows in Fig. 9(b)] are, respectively, shown in Figs. 9(c) and 9(d), which are highly localized at the dimerlike edges together with in-phase and antiphase pressure distributions. Thus, by introducing strong coupling at other types of boundary sites, we can obtain topological boundary states distributed around different types of boundary sites, not limited to A-type lattice sites.

APPENDIX E: INFLUENCE OF THE BOUNDARY SHAPE ON THE APPEARANCE OF BOUNDARY STATES

Now we construct the square-shaped lattice with different boundaries compared with those of the above samples. As shown in Figs. 10(a) and 10(b), there are different types of sites of the unit cell located on the boundaries (i.e., B, C, D, and E sites), apart from the site A. In these cases, the Wannier centers, which are affected by the geometric shapes of the boundaries, do not occur at the outer boundaries. Thus, the truncated boundaries are trivial. According to the eigenpressure spectra for the two lattices [see Figs. 10(a) and 10(b)], we can see that the topological boundary states are absent from the bulk spectral gaps in both Figs. 10(c) and 10(d), consistent with the prediction of the Wannier centers. In fact, for the phase of $t_1/t_2 < 1$, the A-type sites in the unit cell act as the strong coupling centers, the presence of which at the lattice boundaries can induce the emergence of higher-order topological states [as illustrated in Fig. 2(a)]. From these analyses, we can confirm the significant influence of boundary shape on the presence of topological boundary states.

APPENDIX F: THE EIGENFREQUENCY SPECTRA OF THE LATTICES UNDER BOUNDARY DISORDER

Different from the case of bulk disorder, here, we introduce perturbations into the corner and dimerlike edge regions for the samples shown in Figs. 3(a) and 4(a), respectively, with horizontal and slant edges, termed corner disorder and dimerlike edge disorder, respectively. These boundary disorders are schematically shown in the light-green-colored regions of Figs. 11(a) and 11(b). Similar to the case of bulk disorder, the embedded solid cylinders, which are fabricated with epoxy-resin rods in the experiment, are employed to vary the resonant frequencies of the perturbed cavities. The eigenfrequency spectra for the corner and dimerlike edge disordered lattices are, respectively, shown in Figs. 11(c) and 11(d), where the relevant corner and dimerlike edge modes still survive but are both shifted to higher frequencies. In the experiment, with the same method as bulk disorder, the frequency-response spectra for the two square-shaped lattices [shown

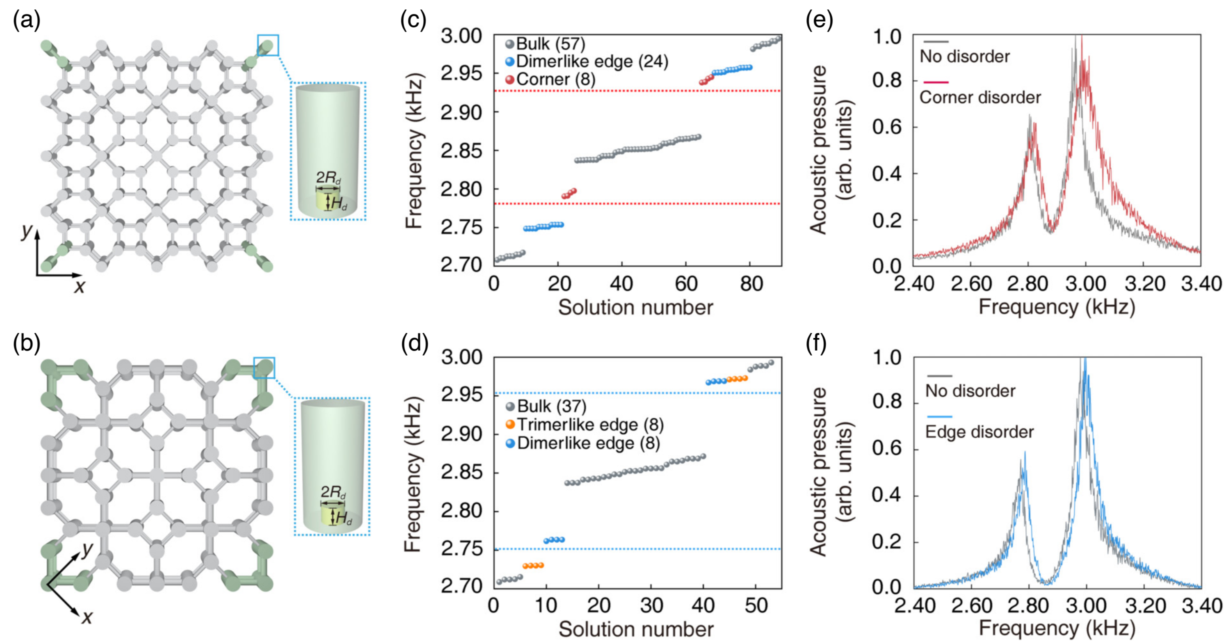

FIG. 11. (a),(b) Schematics of the boundary disordered sonic crystals labeled by colored regions. (c),(d) Eigenfrequency spectra for the cases shown in (a),(b), respectively. (e) Measured spectra of the sonic crystal (a) with corner disorder. (f) Measured spectra of sonic crystal (b) with dimerlike edge disorder. In (e),(f), gray lines indicate the cases of no disorder.

in Figs. 11(a) and 11(b)] are measured from the corner and dimerlike edge cavities, regardless of the perturbed case and the unperturbed case. As shown in Figs. 11(e) and 11(f), comparing the spectra with the cases of no disorder, we observe that these resonant peaks, which are denoted by red and blue lines, move toward higher frequencies. Thus, it turns out that these boundary states are very sensitive to the onsite potential-energy shift on the relevant boundary sites.

APPENDIX G: INTRINSIC ROLES IN THE GENERATION OF DUAL-BAND LOCALIZED STATES

To reveal the essence of the generation of dual-band localized states, we start from the intact square-shaped sonic crystal with nontrivial bulk polarization, as displayed in Fig. 12(a). For the coupling-strength ratio, $t_1/t_2 < 1$, the couplings between the boundary cavities and the adjacent bulk cavities are weak, thus we attempt to divide the composite lattice into different components. We remove the cavities in the bulk [see Fig. 12(b)], leaving only 44 resonators along the boundaries of the sonic crystal, called a hollow sonic crystal, as shown in Fig. 12(c). The eigenfrequency spectra of the above three finite structures are shown in Figs. 12(d)–12(f). Comparing the eigenfrequency spectra [see Fig. 12(f)] with those of the intact acoustic crystal, we notice that the bulk modes vanish, except for a few residual modes distributed only at the outer boundary sites *B*, *C*, *D*, and *E* [see the inset of Fig. 12(f)]. It should be emphasized that the *A*-type lattice sites in the hollow lattice are indispensable for the field patterns of dimerlike edge states, as dictated by the nontrivial Wannier centers; thus, the residual modes only distributed at other types of lattice sites belong to bulk modes. In addition, the corner and dimerlike edge modes for the hollow lattice possess the same eigenfrequencies and quantities as before. These results indicate that the acoustic dual-band higher-order topological states are inherently generated from the local configurations of the boundaries, wherein the eight corner modes are yielded from the eight corner resonators. In essence, the corner, edge, and bulk components can be approximately viewed as independent structure elements, due to the weak couplings of these components with adjacent ones. As verified by the results of bulk and corner disorders in the previous paragraphs, perturbations at the interior bulk region cannot obviously affect the eigenfrequencies of the boundary modes, unless those are applied at relevant boundaries.

APPENDIX H: THE THRESHOLDS OF BULK AND CORNER DISORDERS

In this section, we employ the topologically nontrivial lattice with horizontal edges shown in Fig. 2(a) to discuss the thresholds for different disorders of the corner modes. First, we carry out a tight-binding model calculation of the bulk disordered lattice, where the onsite potential energies at relevant diagonal terms of the Hamiltonian are altered by the disorder strength, δ. As shown in Fig. 13(a), we see

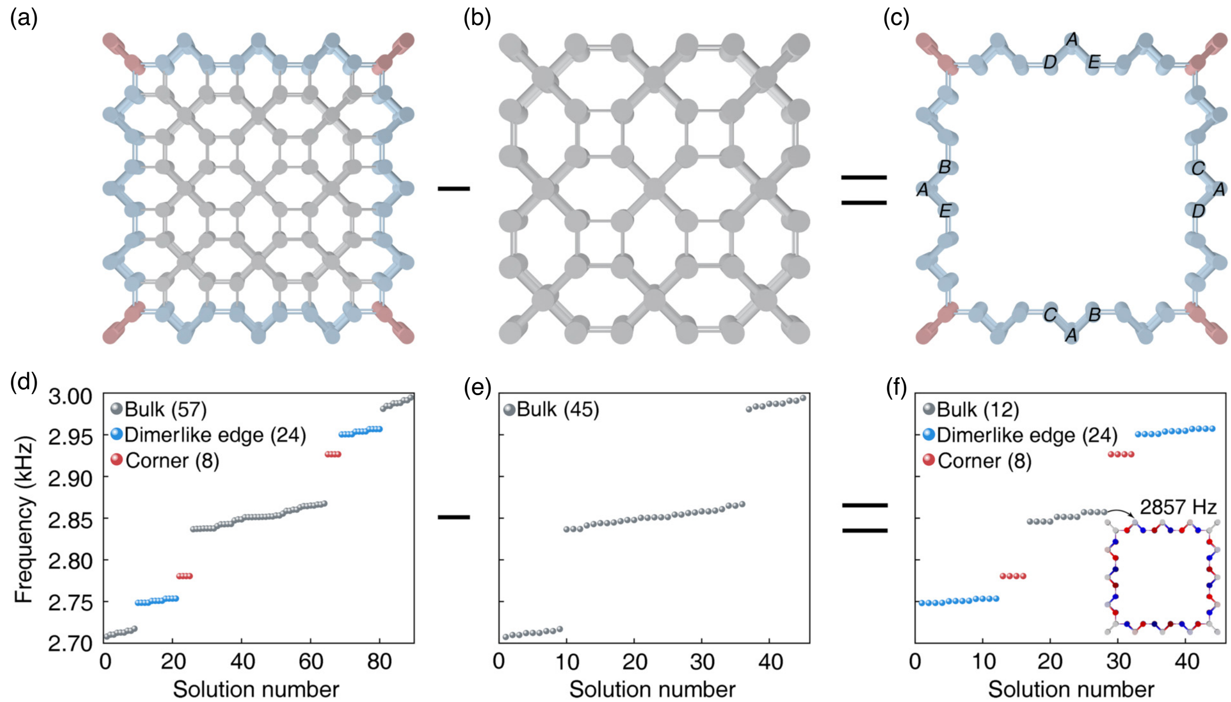

FIG. 12. (a)–(c) Illustrations of the intact square-shaped sonic crystal, the removed bulk, and the hollow sonic crystal, respectively. (d)–(f) Simulated eigenfrequency spectra of the finite lattices shown in (a)–(c), respectively. In (f), inset shows the residual bulk modes distributed at outer boundary sites of the hollow acoustic structure.

that the eigenfrequencies of bulk modes are shifted; this becomes more prominent with an increase in the disorder strength, while those of the boundary modes are stable. At a smaller disorder strength, we can distinguish the boundary modes from the bulk modes. As the strength is enhanced to a value of 0.032, where the corner modes start

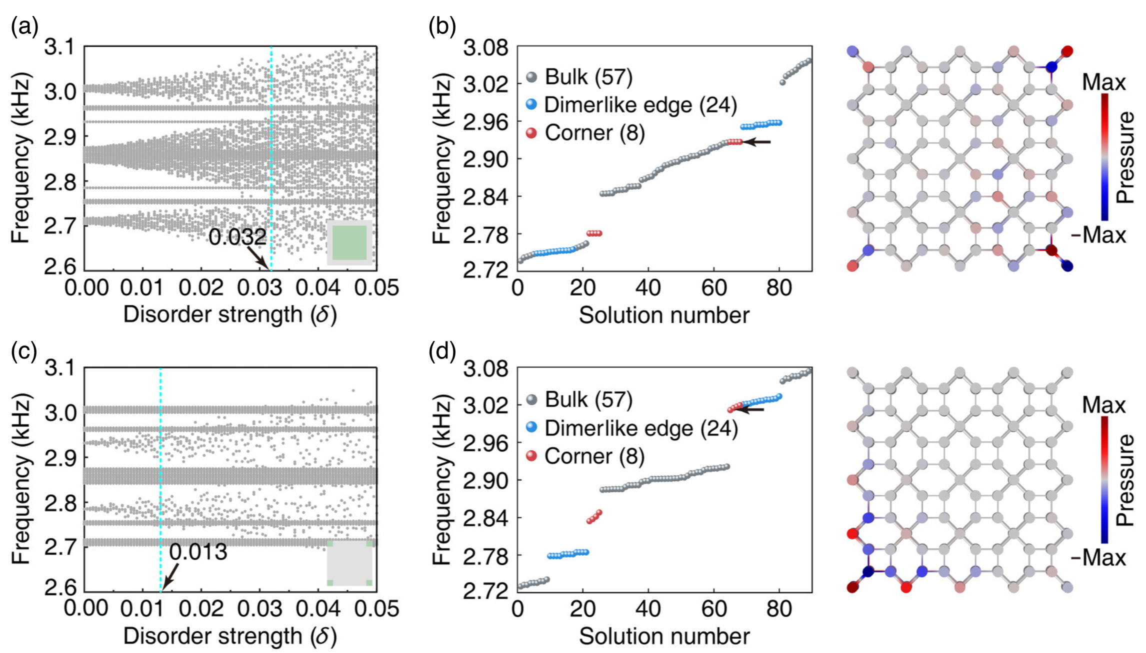

FIG. 13. (a) Calculated eigenfrequencies under different disorder strengths for the bulk disordered lattice. (b) For the threshold strength of bulk disorder, eigenfrequencies and relevant acoustic eigenfields of the corner mode at higher frequency. (c),(d) Similar to (a),(b), but for the case of corner disorder.

to merge into the bulk modes, the threshold emerges. Once the strength exceeds the threshold, these modes become so fully mixed with each other that we can no longer distinguish them at all. With a fixed threshold of 0.032 for bulk disorder, we can assess the maximum height value, that is, 10.2 mm, of the embedded cylinders in the disordered cavities, as the disorder strength is proportional to the volume of the embedded perturbations. Then, we verify the threshold with a numerical simulation by setting random height parameters of the embedded cylinders in the range from 1 to 10.2 mm via COMSOL Multiphysics linked with MATLAB. The eigenfrequencies and eigenpressure fields of the disordered sonic crystal are shown in Fig. 13(b). Specifically, the corner mode at 2926.7 Hz (indicated by a black arrow) is precisely adjacent to the bulk modes, which leads to the slight field penetration into the bulk region for the corner states.

For the case of corner disorder, the same tight-binding calculation and numerical simulation for the nontrivial lattice are carried out, but the perturbations are turned to the corner cavities. In Fig. 13(c), we notice that, as the disorder strength increases, the range of eigenfrequency shifts for the corner modes gradually expands. When the strength reaches a value of 0.013, the corner modes begin to merge with the bulk modes, which represent the threshold. Similarly, based on the threshold, we can determine the range of random heights of the embedded cylinders, spanning from 1 to 4.2 mm. Under these condition, we find that the corner modes with higher eigenfrequencies in Fig. 13(d) directly interact with the edge modes, and the eigenpressure fields for the corner states at 2945.6 Hz exhibit spatial overlap with the adjacent edges, indicating the threshold behavior.

[1] X. Zhang, M. Xiao, Y. Cheng, M.-H. Lu, and J. Christensen, Topological sound, Commun. Phys. **1**, 97 (2018).

[2] Y. Ding, Y. Peng, Y. Zhu, X. Fan, J. Yang, B. Liang, X. Zhu, X. Wan, and J. Cheng, Experimental demonstration of acoustic Chern insulators, Phys. Rev. Lett. **122**, 014302 (2019).

[3] Y.-G. Peng, Y. Li, Y.-X. Shen, Z.-G. Geng, J. Zhu, C.-W. Qiu, and X.-F. Zhu, Chirality-assisted three-dimensional acoustic Floquet lattices, Phys. Rev. Res. **1**, 033149 (2019).

[4] Y. Wu, J. Lu, X. Huang, Y. Yang, L. Luo, L. Yang, F. Li, W. Deng, and Z. Liu, Topological materials for full-vector elastic waves, Nat. Sci. Rev. **10**, nwac203 (2023).

[5] C. He, X. Ni, H. Ge, X.-C. Sun, Y.-B. Chen, M.-H. Lu, X.-P. Liu, and Y.-F. Chen, Acoustic topological insulator and robust one-way sound transport, Nat. Phys. **12**, 1124 (2016).

[6] J. Lu, C. Qiu, L. Ye, X. Fan, M. Ke, F. Zhang, and Z. Liu, Observation of topological valley transport of sound in sonic crystals, Nat. Phys. **13**, 369 (2017).

[7] S.-Y. Yu, C. He, X.-C. Sun, H.-F. Wang, J.-Q. Wang, Z.-D. Zhang, B.-Y. Xie, Y. Tian, M.-H. Lu, and Y.-F. Chen, Critical couplings in topological-insulator waveguide-resonator systems observed in elastic waves, Nat. Sci. Rev. **8**, nwaa262 (2020).

[8] J.-H. Chen, Y. Li, C. Yu, C. Fu, and Z. H. Hang, Realization of the quantum spin Hall effect using tunable acoustic metamaterials, Phys. Rev. Appl. **18**, 044055 (2022).

[9] D. Jia, Y. Ge, H. Xue, S.-Q. Yuan, H.-X. Sun, Y. Yang, X.-J. Liu, and B. Zhang, Topological refraction in dual-band valley sonic crystals, Phys. Rev. B **103**, 144309 (2021).

[10] Z. Wang, Y. Yang, H. Li, H. Jia, J. Luo, J. Huang, Z. Wang, B. Jiang, N. Yang, G. Jin, and H. Yang, Multichannel topological transport in an acoustic valley Hall insulator, Phys. Rev. Appl. **15**, 024019 (2021).

[11] Z.-G. Geng, L.-S. Zeng, Y.-X. Shen, Y.-G. Peng, and X.-F. Zhu, Experimental evidence of selective generation and one-way conversion of parities in valley sonic crystals, J. Appl. Phys. **129**, 074504 (2021).

[12] B. Xie, H.-X. Wang, X. Zhang, P. Zhan, J.-H. Jiang, M. Lu, and Y. Chen, Higher-order band topology, Nat. Rev. Phys. **3**, 520 (2021).

[13] T. Li, J. Du, Q. Zhang, Y. Li, X. Fan, F. Zhang, and C. Qiu, Acoustic Möbius insulators from projective symmetry, Phys. Rev. Lett. **128**, 116803 (2022).

[14] Y. Zhang, J. Tang, X. Dai, S. Zhang, Z. Cao, and Y. Xiang, Design of a higher-order nodal-line semimetal in a spring-shaped acoustic topological crystal, Phys. Rev. B **106**, 184101 (2022).

[15] C. H. Xia, H. S. Lai, X. C. Sun, C. He, and Y. F. Chen, Experimental demonstration of bulk-hinge correspondence in a three-dimensional topological Dirac acoustic crystal, Phys. Rev. Lett. **128**, 115701 (2022).

[16] Z. Pu, H. He, L. Luo, Q. Ma, L. Ye, M. Ke, and Z. Liu, Acoustic higher-order Weyl semimetal with bound hinge states in the continuum, Phys. Rev. Lett. **130**, 116103 (2023).

[17] L. Ye, Q. Ma, S. Yin, D. Yao, H. He, M. Ke, and Z. Liu, Acoustic quadrupolar surface topological semimetals, Phys. Rev. Appl. **19**, 064064 (2023).

[18] X. Huang, J. Lu, Z. Yan, M. Yan, W. Deng, G. Chen, and Z. Liu, Acoustic higher-order topology derived from first-order with built-in Zeeman-like fields, Sci. Bull. **67**, 488 (2022).

[19] D. Wang, Y. Deng, J. Ji, M. Oudich, W. A. Benalcazar, G. Ma, and Y. Jing, Realization of a Z-classified chiral-symmetric higher-order topological insulator in a coupling-inverted acoustic crystal, Phys. Rev. Lett. **131**, 157201 (2023).

[20] P. Zhang, H. Jia, J. Lu, X. Yang, S. Wang, Y. Yang, Z. Liu, and J. Yang, Observations of acoustic Wannier configurations revealing topological corner anomaly, Sci. Bull. **68**, 679 (2023).

[21] F. Gao, Y. G. Peng, X. Xiang, X. Ni, C. Zheng, S. Yves, X. F. Zhu, and A. Alù, Acoustic higher-order topological insulators induced by orbital-interactions, Adv. Mater. **36**, 2312421 (2024).

[22] H. Xue, Y. Yang, F. Gao, Y. Chong, and B. Zhang, Acoustic higher-order topological insulator on a kagome lattice, Nat. Mater. **18**, 108 (2019).

[23] X. Ni, M. Weiner, A. Alù, and A. B. Khanikaev, Observation of higher-order topological acoustic states protected by generalized chiral symmetry, Nat. Mater. **18**, 113 (2019).

[24] L. Zhang, Y. Yang, M. He, H. X. Wang, Z. Yang, E. Li, F. Gao, B. Zhang, R. Singh, J. H. Jiang, and H. Chen, Valley kink states and topological channel intersections in substrate-integrated photonic circuitry, Laser Photon. Rev. **13**, 1900159 (2019).
[25] Y. Liu, S. Leung, F.-F. Li, Z.-K. Lin, X. Tao, Y. Poo, and J.-H. Jiang, Bulk–disclination correspondence in topological crystalline insulators, Nature **589**, 381 (2021).
[26] L. Ye, C. Qiu, M. Xiao, T. Li, J. Du, M. Ke, and Z. Liu, Topological dislocation modes in three-dimensional acoustic topological insulators, Nat. Commun. **13**, 508 (2022).
[27] Z. Xiong, Z.-K. Lin, H.-X. Wang, X. Zhang, M.-H. Lu, Y.-F. Chen, and J.-H. Jiang, Corner states and topological transitions in two-dimensional higher-order topological sonic crystals with inversion symmetry, Phys. Rev. B **102**, 125144 (2020).
[28] D. Liao, Z. Zhang, Y. Cheng, and X. Liu, Engineering negative coupling and corner modes in a three-dimensional acoustic topological network, Phys. Rev. B **105**, 184108 (2022).
[29] Y. Qi, C. Qiu, M. Xiao, H. He, M. Ke, and Z. Liu, Acoustic realization of quadrupole topological insulators, Phys. Rev. Lett. **124**, 206601 (2020).
[30] W. A. Benalcazar, T. Li, and T. L. Hughes, Quantization of fractional corner charge in C_n-symmetric higher-order topological crystalline insulators, Phys. Rev. B **99**, 245151 (2019).
[31] G. Duan, S. Zheng, Z.-K. Lin, J. Jiao, J. Liu, Z. Jiang, and B. Xia, Numerical and experimental investigation of second-order mechanical topological insulators, J. Mech. Phys. Solids **174**, 105251 (2023).
[32] X. Zhang, Z.-K. Lin, H.-X. Wang, Z. Xiong, Y. Tian, M.-H. Lu, Y.-F. Chen, and J.-H. Jiang, Symmetry-protected hierarchy of anomalous multipole topological band gaps in nonsymmorphic metacrystals, Nat. Commun. **11**, 65 (2020).
[33] Z. Yue, Z. Zhang, H.-X. Wang, W. Xiong, Y. Cheng, and X. Liu, Glided acoustic higher-order topological insulators based on spoof surface acoustic waves, New J. Phys. **24**, 053009 (2022).
[34] H. Xue, Y. Yang, G. Liu, F. Gao, Y. Chong, and B. Zhang, Realization of an acoustic third-order topological insulator, Phys. Rev. Lett. **122**, 244301 (2019).
[35] X. Zhang, B.-Y. Xie, H.-F. Wang, X. Xu, Y. Tian, J.-H. Jiang, M.-H. Lu, and Y.-F. Chen, Dimensional hierarchy of higher-order topology in three-dimensional sonic crystals, Nat. Commun. **10**, 5331 (2019).
[36] Z.-Z. Yang, X. Li, Y.-Y. Peng, X.-Y. Zou, and J.-C. Cheng, Helical higher-order topological states in an acoustic crystalline insulator, Phys. Rev. Lett. **125**, 255502 (2020).
[37] M. Weiner, X. Ni, M. Li, A. Alù, and A. B. Khanikaev, Demonstration of a third-order hierarchy of topological states in a three-dimensional acoustic metamaterial, Sci. Adv. **6**, eaay4166 (2020).
[38] Q. Wu, H. Chen, X. Li, and G. Huang, In-plane second-order topologically protected states in elastic kagome lattices, Phys. Rev. Appl. **14**, 014084 (2020).
[39] Z. Yue, D. Liao, Z. Zhang, W. Xiong, Y. Cheng, and X. Liu, Experimental demonstration of a reconfigurable acoustic second-order topological insulator using condensed soda cans array, Appl. Phys. Lett. **118**, 203501 (2021).
[40] D. Liao, Z. Yue, Z. Zhang, H.-X. Wang, Y. Cheng, and X. Liu, Observations of Tamm modes in acoustic topological insulators, Appl. Phys. Lett. **120**, 211701 (2022).
[41] W.-J. Yang, Z.-Z. Yang, X.-Y. Zou, and J.-C. Cheng, Characterization and experimental demonstration of corner states of boundary-obstructed topological insulators in a honeycomb lattice, Phys. Rev. B **107**, 174101 (2023).
[42] W. Xiong, S. Wang, Z. Zhang, H. Zhang, Y. Cheng, and X. Liu, Observation of multiple off-site corner states induced by next-nearest-neighbor coupling in a sonic crystal, Phys. Rev. B **109**, 024305 (2024).
[43] X.-Y. Liu, Y. Liu, Z. Xiong, H.-X. Wang, and J.-H. Jiang, Higher-order topological phases in bilayer phononic crystals and topological bound states in the continuum, Phys. Rev. B **109**, 205137 (2024).
[44] J. Li, C. Deng, K. Zhang, Q. Lu, and H. Yang, Higher-order topological states in dual-band valley sonic crystals, Appl. Phys. Lett. **123**, 253101 (2023).
[45] Y. Chen, J. Zhu, and Z. Su, Topology optimization of a second-order phononic topological insulator with dual-band corner states, J. Sound Vib. **544**, 117410 (2023).
[46] L. Fan, Y. Chen, J. Zhu, and Z. Su, Topological interface and corner states of flexural waves in metamaterial plates with glide-symmetric holes, J. Sound Vib. **595**, 118795 (2025).
[47] M. Yan, X. Huang, L. Luo, J. Lu, W. Deng, and Z. Liu, Acoustic square-root topological states, Phys. Rev. B **102**, 180102 (2020).
[48] S.-Q. Wu, Z.-K. Lin, Z. Xiong, B. Jiang, and J.-H. Jiang, Square-root higher-order topology in rectangular-lattice acoustic metamaterials, Phys. Rev. Appl. **19**, 024023 (2023).
[49] Z.-G. Geng, Y.-X. Shen, Z. Xiong, L. Duan, Z. Chen, and X.-F. Zhu, Quartic-root higher-order topological insulators on decorated three-dimensional sonic crystals, APL Mater. **12**, 021108 (2024).
[50] Y. Yang, J. Lu, M. Yan, X. Huang, W. Deng, and Z. Liu, Hybrid-order topological insulators in a phononic crystal, Phys. Rev. Lett. **126**, 156801 (2021).
[51] W. Sun, L. Luo, Y. Huang, J. Peng, D. Zhao, Y. Yao, F. Wu, and X. Zhang, Observation of acoustic hybrid-order topological insulator induced by non-Hermiticity and anisotropy, Phys. Rev. B **109**, 134302 (2024).
[52] F. Liu, H.-Y. Deng, and K. Wakabayashi, Topological photonic crystals with zero Berry curvature, Phys. Rev. B **97**, 035442 (2018).
[53] J. Liang, R. Zheng, Z. Lu, J. Pan, J. Lu, W. Deng, M. Ke, X. Huang, and Z. Liu, Corner states and particle trapping in waterborne acoustic crystals, Appl. Phys. Lett. **124**, 101704 (2024).
[54] F. Liu and K. Wakabayashi, Novel topological phase with a zero Berry curvature, Phys. Rev. Lett. **118**, 076803 (2017).